The 6th International Supercritical CO_2 Power Cycles Symposium
March 27 - 29, 2018, Pittsburgh, Pennsylvania

Numerical Simulations of CO2 Compressors: Subcritical Inlet Conditions

Ashvin Hosangadi
Vice President
CRAFT Tech.
Pipersville, PA, USA

Zisen Liu
Research Scientist
CRAFT Tech.
Pipersville, PA, USA

Timothy Weathers
Assistant Research Scientist
CRAFT Tech.
Pipersville, PA, USA

Vineet Ahuja
Senior Research Scientist
CRAFT Tech.
Pipersville, PA, USA

ABSTRACT

A generalized numerical framework to model phase change at subcritical conditions in CO_2 over a wide range of conditions is presented in this paper. This model is implemented with an advanced numerical framework that features independent mass transport equations for liquid and vapor CO_2, and can also be extended to include contaminants. A table look-up procedure based on the NIST database was implemented for both supercritical and subcritical conditions. A key contribution here is the extension of the look-up procedure to subcritical conditions using saturation curves as bounding lines to distinguish between liquid and vapor properties. Phase change is triggered by the difference between the local values of pressure and saturation pressure and do not require the phase change physics (i.e. condensation or vaporization) to be specified apriori.

Rigorous validation of the phase change framework is presented for condensation in CO_2 using test data in a De Laval nozzle. The comparisons between computations and test data include; condensation onset locations, Wilson line, and nozzle pressure profiles as a function of inlet pressures. In general, the comparisons for all these quantities is very good. The comparisons are closer at higher pressures since the condensation time scales become smaller and the flow reaches equilibrium earlier. Based on these results it may be concluded that the equilibrium model for phase change provides adequate engineering fidelity.

The phase change model has also been demonstrated for the Sandia test loop compressor for three different sets of inlet conditions: Case 1) Supercritical inlet conditions, Case 2) 2-phase liquid-vapor mixture at inlet where the inlet is subcritical at a temperature of 290 K, and Case 3) Liquid inlet conditions at a temperature of 295 K. At supercritical inlet conditions (Case 1) the phase change model predicts condensation at the leading edge and the trailing edge of the impeller as the temperature drops relatively faster than the pressure making the fluid sub-cooled. However, the phase change characteristics show a dramatic change when the inlet has substantial liquid mass at subcritical conditions. For Case 2 (two-phase inlet) and Case 3 (liquid inlet), we observe cavitation near the leading edge as the relative variations of pressure and temperature change. At these subcritical inlet conditions with liquid inflow, the pressure drop is more than the saturation pressure drop from the lower temperature, as the flow accelerates round the leading edge, leading to vaporization or cavitation. We postulate that reduced compressibility in liquid suppresses the temperature reduction at these conditions. While cavitation is a concern due to its potential for damage and erosion, the effect of cavitation is mitigated by the fact that the liquid to vapor density ratios at these elevated temperatures are much smaller (order of 4) thus reducing the pressure amplitudes from cavitation collapse.

INTRODUCTION

The compressors in supercritical CO_2 (SCO_2) power cycles are compact, rotate at high speeds and are designed to operate near the critical point (304.12K, 7.37 MPa) [1]. At its design point and at other supercritical inlet conditions two phase effects for pure CO2 systems are expected to be minimal although condensation may potentially occur in a small region near the leading edge. However, more substantial two phase effects are possible when the inlet conditions can show larger fluctuations as is the case for air-cooled cycles and compressor inlet temperatures are subject to variations in ambient conditions [2]. Furthermore, transient operating conditions particularly at start-up also experience subcritical conditions since the critical temperature for CO_2 is generally higher than the ambient temperature and initial conditions in the loop are both subcritical in temperature and pressure [3]. Thus the compressor may need to operate within the saturation dome during start-up until the conditions become supercritical and it is important to characterize the performance and stability of the compressor under two-phase conditions. We note that at subcritical inlet conditions two-phase effects can manifest themselves as either vaporization or condensation; in fact the precise nature of the phase change will be governed by the differences between the local pressure and the saturation pressure corresponding to the local temperature.

Multi-phase effects become even more important if the working fluid is not pure CO_2 but instead has contaminants such as water or CO present [4]. The variation of the mixture critical point with composition can be extremely non-linear and substantially exceed the individual critical pressures particularly when components have disparate critical properties and volatilities [5]. This necessitates that the numerical framework be versatile and can be extended to have multiple species with generalized phase change models that allow for condensation/vaporization within a multi-component framework.

Condensation modeling in the literature at near critical conditions has typically involved an elaborate non-equilibrium framework wherein the temperature and velocity of the dispersed phase is solved for independently of the continuum fluid with drag, heat transfer and phase change source terms to drive it to equilibrium. In this framework, homogeneous condensation nuclei are generated based on classical nucleation theory, where the nucleation rate is a function of the Gibbs free energy of formation and the mean thermal energy [6]. Subsequently the size of these condensation nuclei can change due to condensation and vaporization where the source terms for phase change are given by non-equilibrium formulations such as the generalized Hertz-Knudsen model [7].

Simpler equilibrium models where common temperature and velocity are assumed have also been demonstrated in the literature and the authors have presented detailed validation for cavitation in cryogenic fluids using such a model [8]. This model requires the solution of additional conservation equations that keep track of liquid and vapor mass separately. Phase change is triggered by the differences between the local pressure and saturation pressure corresponding to the local sub-critical temperature of the fluid. Finite rate phase change models that permits both condensation and vaporization provide a seamless formulation that does not require apriori specification of fluid phase.

The focus of this paper is on modeling compressor performance for conditions that span near critical to sub-critical conditions within the saturation dome using the equilibrium phase change model [8]. Detailed validation of numerical results for CO_2 condensation at high inlet pressures in a De Laval nozzle are compared with data published by Lettieri [9]. We compare condensation locations, Wilson line, and pressure distribution in nozzle for various inlet conditions ranging from 59-85 bar at temperatures from 311-314 K.

Subsequently, we present multi-phase results for compressor performance in the Sandia test loop [1] at three different conditions; a) Supercritical inlet conditions, b) 2-Phase inlet conditions at a low subcritical temperature of 290 K, and c) liquid inflow conditions at a subcritical temperature of 295 K where the inlet pressure is varied from 63 bar to 72 bar. We observe significant difference in the flow characteristics between these cases with condensation being observed at the supercritical inlet condition while cavitation occurs at lower subcritical inlet temperatures. These flow characteristics are discussed in detail in this paper.

In the sections to follow, we provide a brief overview of the numerical framework for real fluid thermodynamics as well as the procedure for property look-up spanning subcritical thru supercritical regimes. Details of the phase change model are provided. This is followed by a discussion of CO2 condensation in a De Laval nozzle to validate the numerical results with test data from Lettieri [9]. Results for subcritical performance of the Sandia compressor are discussed subsequently followed by a conclusions section.

Real Fluid Numerical Framework

To define a robust framework for real fluid systems (where density variations can be small and stiff) the equations system solves for the primitive variables comprising pressure and temperature as given by the vector $Q_v = \left[p, u, v, w, T, y_g, k, \varepsilon \right]^T$. The variable y_g represents the vapor mass fraction, while k and ε represent the turbulence transport. The conservation equations are written in coupled matrix form as [10]:

$$\Gamma_p \frac{\partial Q_v}{\partial \tau} + \frac{\partial E}{\partial x} + \frac{\partial F}{\partial y} + \frac{\partial G}{\partial z} = S + D_v \tag{1}$$

where the matrix Γ_p defines the transformation from conservative to primitive variables and also includes acoustic preconditioning for accuracy/robustness as discussed later; E, F and G are the flux vectors; S represents the source terms (e.g., from phase change); and D_v represents the viscous fluxes.

We note that in Eqn. (1) we have added an additional equation for the conservation of the vapor phase (the liquid phase is obtained from the mixture mass from global continuity). This permits us to account for phase change (either condensation or vaporization) as the local conditions dictate without apriori accounting for the subcritical or supercritical properties of the fluid. In the more general case where the CO2 may not be pure, the framework can be extended seamlessly by adding transport equations for contaminant species. The density of the local fluid which may be composed of both liquid and vapor phases is written in a general fashion as:

$$\begin{aligned} \rho &= \rho_g \phi_g + \rho_L \phi_{L,} \\ \phi_i &= \frac{y_i \rho}{\rho_i} \quad (i = \text{ Vapor g, or Liquid L}) \end{aligned} \tag{2}$$

The matrix Γ_p is written as [15]:

$$\Gamma_p = \begin{pmatrix} \beta\rho_p & 0 & 0 & 0 & \rho_T & \rho_{y_G} & 0 & 0 \\ u\beta\rho_p & \rho & 0 & 0 & u\rho_T & u\rho_{y_G} & 0 & 0 \\ v\beta\rho_p & 0 & \rho & 0 & v\rho_T & v\rho_{y_G} & 0 & 0 \\ w\beta\rho_p & 0 & 0 & \rho & w\rho_T & w\rho_{y_G} & 0 & 0 \\ H\beta\rho_p - (1-\rho h_p) & \rho u & \rho v & \rho w & H\rho_T - (1-\rho h_T) & H\rho_{y_G} + \rho h_{y_G} & 0 & 0 \\ y_g\beta\rho_p & 0 & 0 & 0 & y_g\rho_T & \rho & 0 & 0 \\ k\beta\rho_p & 0 & 0 & 0 & k\rho_T & k\rho_{y_G} & \rho & 0 \\ \varepsilon\beta\rho_p & 0 & 0 & 0 & \varepsilon\rho_T & \varepsilon\rho_{y_G} & 0 & \rho \end{pmatrix} \tag{3}$$

We point out two important salient features of the formulation. First, the derivatives of density and enthalpy with respect to pressure and temperature are written in completely general form as ρ_P, ρ_T, h_P, h_T. This allows the sharp variations of these derivatives near the critical point to be modeled faithfully and would potentially lead to more accurate results near the critical point compared to other models in the literature [11]-[13]. Furthermore, the numerical formulation only requires the specification of density and enthalpy for

each phase as functions of pressure and temperature, $\rho = f(P,T)$ and $h = g(P,T)$. This permits the user to easily specify different EoS models or a tabular look-up.

The second point to note is that flows at high supercritical pressures or flows with phase change show large variations in acoustic speed and are numerically stiff. The matrix Γp reflects the use of preconditioning techniques (as represented by the factor β) following the work of Merkle and co-workers [14]. Briefly, the preconditioning rescales the acoustic speed of sound locally to make it the order of the velocity magnitude and thereby alleviating numerical stiffness. This is particularly useful in integrating across a vapor/liquid interface as would occur if condensation occurs in the compressor flow. For unsteady flows, an iterative "dual-time" stepping is employed at each time step to get time-accurate solutions [15].

The real fluid framework is implemented within the CRUNCH CFD® code [16]; this is an unstructured flow solver based on a cell-vertex method that supports mixed multi-element cell types. Two equation turbulence models based on k-ϵ, as well as k-ω SST, are available for steady RANS simulations. Unsteady hybrid RANS-LES models [17] which have been extensively validated for real fluid flows are also available. For efficient computation of large 3D problems, an MPI based parallel framework for distributed memory systems has been implemented along with an implicit time-marching solution procedure.

NIST TABLE LOOK-UP PROCEDURE

As discussed earlier, the numerical formulation requires the specification of density, enthalpy, and their derivatives ρ_P, ρ_T, h_P, h_T as a function of local pressure and temperature. As an alternative to analytical EoS models, a table-look-up procedure generated from NIST database [18] has been implemented for these thermodynamic properties as well as transport properties i.e. viscosity μ, and thermal conductivity k. For supercritical conditions, the extraction of property values from the table is relatively straightforward although care must be taken to maintain adequate resolution in the table near the critical point; we compare the look-up values with the values from NIST later below.

The situation is much more complex at subcritical conditions, where both liquid and vapor exist at the saturation pressure and temperature, and the table look-up procedure needs to identify each state independently. Note that the equation system we solve for tracks both the liquid and vapor component of the fluid independently and is consistent with this physics. The NIST table look-up procedure was further enhanced for the subcritical regime. Specifically, the saturation curves are generated from the NIST database and read in. For subcritical conditions, we obtain the separate liquid and vapor values (density, enthalpy and derivatives) independently at the saturation pressure corresponding to the local fluid temperature. Recognizing that the local pressure may be out of equilibrium with the saturation pressure, phase change is initiated and source terms are added to drive the system to equilibrium. When pressure exceeds the vapor pressure vapor is condensed to liquid and vice versa vapor is generated when pressure is below the vapor pressure. These phase changes source terms are described later below.

The CO_2 property table has been generated over a range relevant to the compressor operational regime map and spans the sub-critical to supercritical range. The temperature range is from 290 K to 330 K with 701 points in temperature, the pressure range is from 4 to 14 MPA with 501 points in pressure, and the saturation curve is defined by 101 points till the critical point. We note that the table features a high resolution (particularly in temperature). This is due to the fact that the variation of properties particularly in the derivatives of density and enthalpy are very large with discontinuous spiky behavior near the critical point. Hence a high resolution is used to accurately model the properties in this range. We also point out that the numerical scheme did not exhibit any instability as the resolution of the table was increased; in fact, we have computed with a table resolution of 3001 points in the temperature range of 290 K to 330 K without any numerical issues. In contrast, Ameli et al. [13] report restrictions to table resolution to avoid numerical instabilities they employed tables with lower resolution.

The properties obtained from the table look-up calls from the numerical solver are compared directly with the values from NIST to verify its providing the correct value. Figure 1 shows the density and enthalpy at various pressures ranging from a subcritical 5.5 MPA (black line), near critical (red line), to a supercritical pressure of 11.5 MPA (blue line). The symbols are the values from NIST while the solid lines are the values

from the table look-up procedure. We note that the table look-up values match perfectly with the NIST values even at the critical value and it identifies the phase transition and jump in liquid and vapor values correctly (black line).

In Figure 2 we plot the derivatives of density and enthalpy for the table look-up procedure. We note the very large values of derivatives at the critical point (red line) and most importantly the table look-up procedure provides the correct value despite the spiky behavior. At supercritical pressures, the derivatives have a peak at the pseudo-critical temperatures which is also resolved accurately by the table look-up procedure.

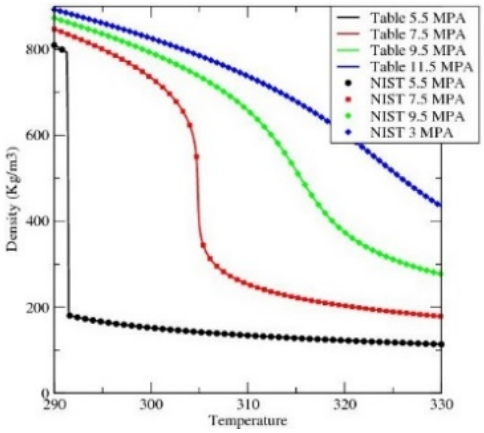

(a) Density

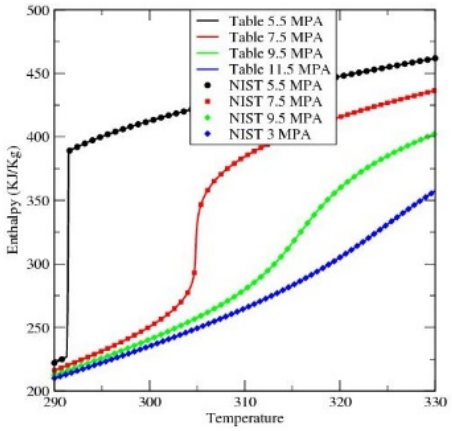

(b) Enthalpy

Figure 1: Table Look-up Comparison with NIST for Density and Enthalpy at Various Pressures

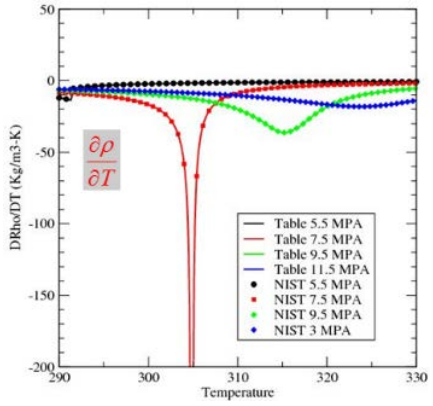

(a)

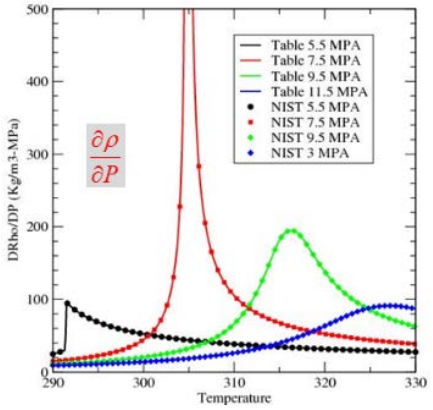

(b)

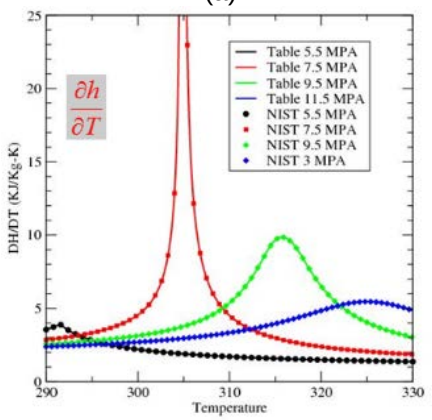

(c)

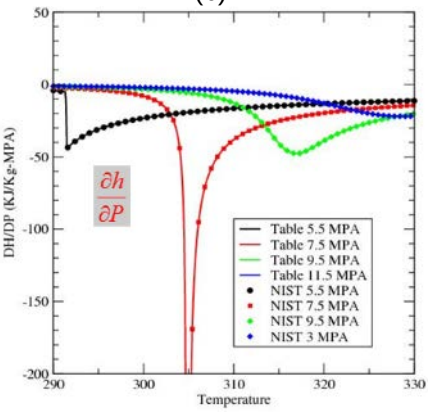

(d)

Figure 2: Table Look-up Comparison with NIST: for Derivatives of Density and Enthalpy

Equilibrium Phase Change Model

To model phase change in CO_2 "two-fluid" framework is required wherein separate mass conservation transport equations for liquid and vapor are solved for as shown in Eqn (1). The two components are assumed to be in equilibrium locally with an identical velocity and hence only mixtures conservation equations for the momentum and energy need to be solved. Phase change is driven by local conditions: a finite rate phase change model that compares the difference between the fluid pressure relative to vapor pressure was based on local temperature of fluid. In Equation (4) below the net mass transfer is given by m_t and is comprised of vaporization and condensation terms that drive the solution to pressure equilibrium:

$$
\begin{aligned}
& m_t = K_f \rho_L \phi_L + K_b \rho_g \phi_g \\
& K_b = \begin{bmatrix} 0 & p < p_v \\ \dfrac{1}{\tau_b^*} & [\dfrac{p - p_v}{\frac{1}{2}\rho_\infty V_\infty^{\,2}}] \quad p > p_v \end{bmatrix}; \quad K_f = \begin{bmatrix} 0 & p > p_v \\ \dfrac{1}{\tau_f^*} & [\dfrac{p - p_v}{\frac{1}{2}\rho_\infty V_\infty^{\,2}}] \quad p < p_v \end{bmatrix} \\
& \tau_f = \text{Time scale for vapor formation (s)} \\
& \tau_b = \text{Time scale for liquid condensation (s)} \\
& \mathrm{V}_\infty = \text{Reference velocity scale} \\
& \mathrm{L}_\infty = \text{Reference length scale} \\
& \tau_f^* = \tau_f \left(\frac{V_\infty}{L_\infty} \right), \quad \tau_b^* = \tau_b \left(\frac{V_\infty}{L_\infty} \right)
\end{aligned}
\tag{4}
$$

We note that the phase change source terms in Equation (4) allow the user to model either condensation or vaporization (cavitation) with the physics being driven by the difference between the local pressure and saturation pressure corresponding to the local temperature. The time scales for vaporization and condensation respectively (τ_f, τ_b) are specified as constants and are not a function of the local properties.

Typically, the time scales for phase change are chosen to be as small as possible (for rapid phase change) to drive the two-phase flowfield to equilibrium while maintaining numerical stability. In the present calculation, the time scales were specified to be 10^{-3} seconds. Despite it apparent simplicity the model is very versatile in that it can seamlessly simulate both condensation and vaporization based on local conditions and in particular does not require apriori specification of the phase change physics.

VALIDATION FOR CO_2 CONDENSATION IN DE LAVAL NOZZLE

Detailed validation of the equilibrium phase change model is presented for condensation in CO_2 using the test data generated by Lettieri et al. [9] ; the experimental test set up comprises a blow-down facility where a high-pressure charge tank exhausts flow through a De Laval nozzle test section. The nozzle length is 0.155 m and the throat area is 20 mm^2. The outlet to throat and inlet to throat area ratios are 1.3 and 4.1 respectively. Figure 3 shows the CFD grid used in the present study; the grid has substantial clustering axially starting upstream of the nozzle throat. Grid clustering is also present at the nozzle wall to capture the boundary layer. Specific details on the grid resolutions are provided later below. NIST table properties were generated over a range of 245-315 K and 1.5-8.5 MPa. Tw different resolutions were studied: a) a "medium" resolution table with 1001 points in temperature, 3001 points in pressure, 501 points for saturation curve and b) a "high" resolution table with 3001 points in temperature, 5001 points in pressure and 1501 points for saturation curve. No appreciable differences were observed in the solutions for these two tables on identical grids.

Figure 3: CFD grid for De Laval Nozzle Configuration from Lettier et al. [9] used in Validation Study.

The flow conditions that are computed correspond to test data in [9] are shown below in Table 1. The inlet pressures range from 58.96 bar to 84.74 bar with temperatures in a narrow band from 311.99 K to 314.67 K. As the high-pressure flow at the inlet expands in the nozzle throat, the flow becomes supersonic and the temperature becomes subcritical resulting in the onset of condensation. The condensation onset progressively moves closer to the throat as the pressure increases and in fact at the highest two pressure values (Case 5a and Case 4a) goes upstream of the throat into the converging section.

In general, the difficulty in obtaining a numerical solution increased as the pressure increased; typically the requirements for axial resolution around the condensation onset point went up as the inlet pressure increased both because the density ratio at the condensation onset increased and the condensation was more rapid. Three different grid resolutions were attempted: a) coarse grid resolution with spacing of 0.1 mm in throat region, b) medium resolution of 0.05 mm, and c) fine grid resolution of 0.0025 mm. With the coarse grid resolution, we were only able to obtain solution for the lowest pressure Case 8a while with the medium resolution we were able to get solution for Cases 8a-6a. The fine grid was needed for Case 4a. The solutions shown here were all obtained on the fine grid with a spacing of 0.0025 mm in the throat region and with the higher resolution NIST table.

Figure 4 compares the CFD solution for condensation with flow visualization data from Lettieri et al. [9]. The CFD solutions plot the liquid volume fraction for the various inlet conditions and are shown on the right. The flow visualization from the test is shown on the left. We observe that CFD solution qualitatively predict the correct trend for condensation onset with inlet pressure; as the inlet pressure increases the condensation moves upstream. The condensation onset estimate in the CFD solutions is shown as a black line in the figures on the right. A quantitative comparison of the condensation onset is made in Figure 5 which confirms that the CFD predictions are very good. At the lowest pressure of 58.96 bar, the condensation onset is slightly earlier than the data while at the highest pressure of 84.74 bar the condensation onset occurs slightly later. However, despite these minor differences the shape of the condensation onset curve is very close to the test curve including the change in slope at the highest pressure of 84.74 bar.

Table 1: Nozzle Inlet Conditions Numerically Computed for Validation with Test Data

Case	P_T (bar)	T_T(K)	S (J/Kg-K)	P_T/P_c	T_T/T_c	S/S_c
8a	58.96	314.67	1862.6	0.7992	1.0346	1.298
7a	65.35	311.99	1796.2	0.8858	1.0258	1.252
6a	73.53	313.60	1736.2	0.9767	1.0311	1.210
5a	79.99	313.94	1669.8	1.0842	1.0322	1.164
4a	84.74	313.88	1599.0	1.1486	1.0321	1.114

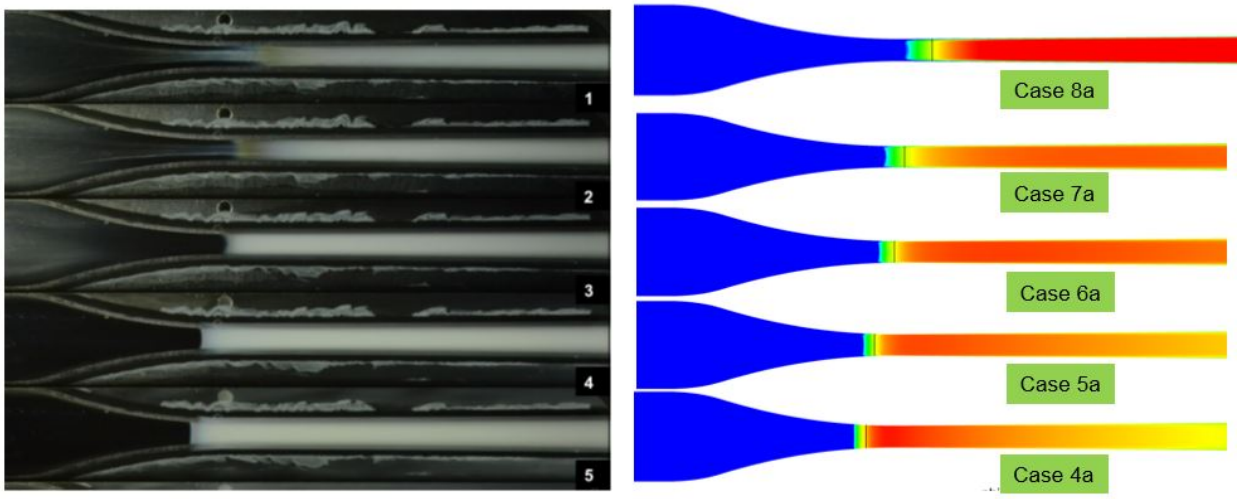

Figure 4: Comparison of Condensation (Liquid Volume Fraction) prediction from CFD with Experimental Flow Visualization Data from [9]

The computed temperature profiles in the nozzle are plotted in Figure 6 as solid lines. We observe that as the inlet pressure increases the temperature downstream of the throat also increases. This is due to the fact that the mass of the liquid condensate (or liquid volume fraction) increases with pressure and the corresponding enthalpy change from the larger liquid mass results in higher fluid temperatures downstream of the throat. The condensation onset points are indicated by dotted line at the onset point. The temperature at the onset point is obtained at the intersection point of the dotted onset-line with their corresponding temperature curve and used to plot the Wilson line.

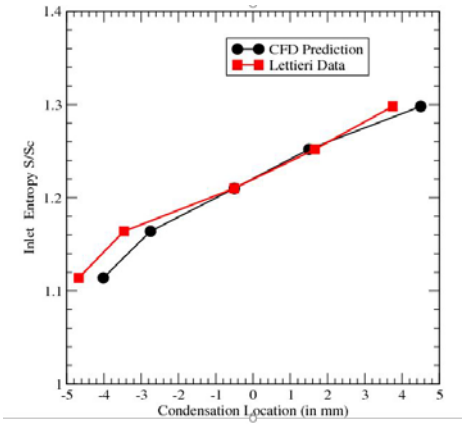

Figure 5: Quantitative Comparison of Condensation Onset Predicted by CFD with Test Data from [9]

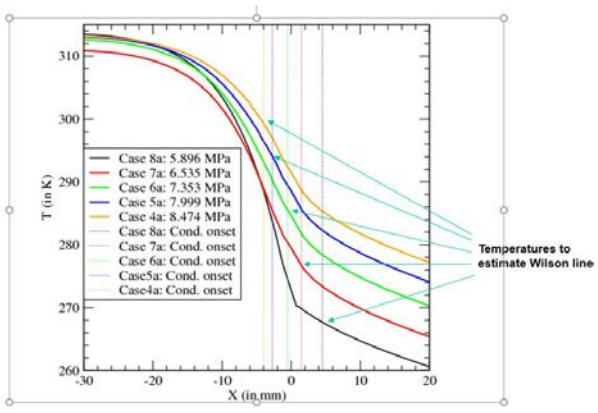

Figure 6 Temperature Profile Along Nozzle with Location of Condensation for Each Case Shown as Dashed Lines

The numerically computed Wilson line is compared with the test data in Figure 7. The red square symbols are the test data from Lettieri et al. [9] while the black circles are the CFD values computed as described in the previous paragraph. We note that the CFD predictions overall under-predict the test data marginally but the variation with inlet entropy matches the data well with the CFD curve nearly parallel to the test curve. As the inlet entropy gets closer to the critical value, the comparison with the test data gets better because

the condensation onset is rapid and the implied time scale in the equilibrium formulation becomes a very good approximation to the non-equilibrium process. At the lower inlet pressures (higher entropy), the non-equilibrium lag in condensation onset is more significant we observe the CFD data is underpredicting the sub-cooling that is present before condensation onset takes place.

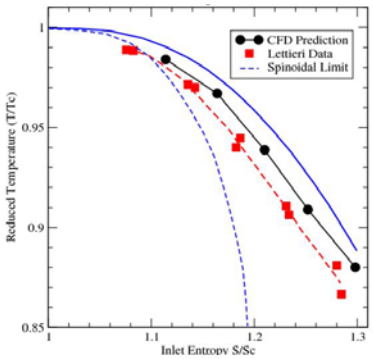

Figure 7: Wilson Line Computed from CFD Compared with Test Data from [9]

Finally, we compare the computed pressure profiles in the nozzle with measured pressure values in Figure 8. On the y-axis, the local static pressure is plotted normalized with the inlet total pressure. We observe that at the lower pressures of 58.96 bar and 65.35 bar the pressure comparisons show differences around the condensation onset point but come closer further downstream as the test data also reaches full equilibrium. This is consistent with the observations for the Wilson line which also indicated that we were underpredicting the sub-cooling at the lower inlet pressures. As the inlet pressure becomes higher, the comparison of pressure is quite good although a slight difference is still observed near the condensation onset. In general the pressure comparison are consistent with the observations for the Wilson line where we noted that the equilibrium phase change formulation improves in accuracy as the condensation time scales become smaller leading to rapid onset.

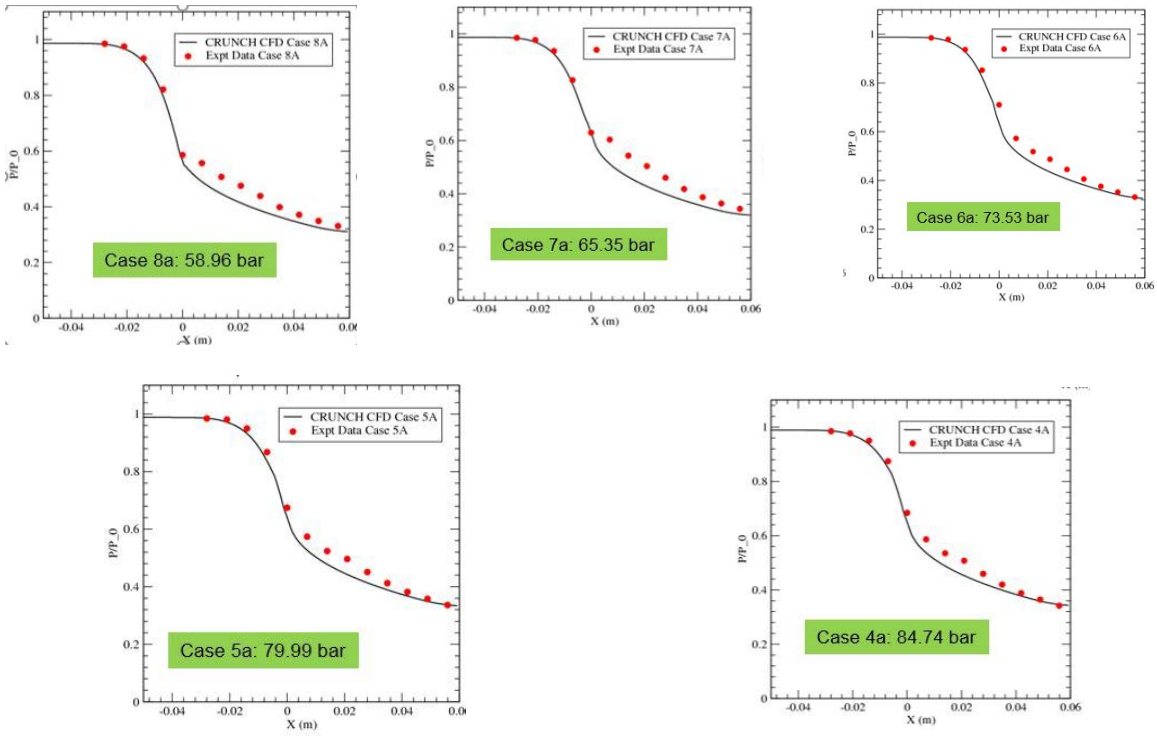

Figure 8: Comparisons of Pressure Profile in Nozzle with Test Data at Various Inlet Conditions

Compressor Simulations at Sub-Critical Inlet Conditions

Simulations of the compressor in Sandia's test loop [1] for near critical and sub-critical inlet conditions are discussed in this section. The compressor section of the test loop and the impeller test article is shown in Figure 9(a); the impeller leads to a vaned diffuser that exhausts into a volute. We note that the CFD simulation ends at the diffuser exit and does not model the losses in the volute and exit pipe. Furthermore, the impeller has pump out vanes on its back side in the leakage passage; the CFD model did not model the pump-out vanes or the leakage. Thus, the efficiency calculations in the CFD simulations cannot be compared directly without adding an estimate for the leakage and pump-out vanes.

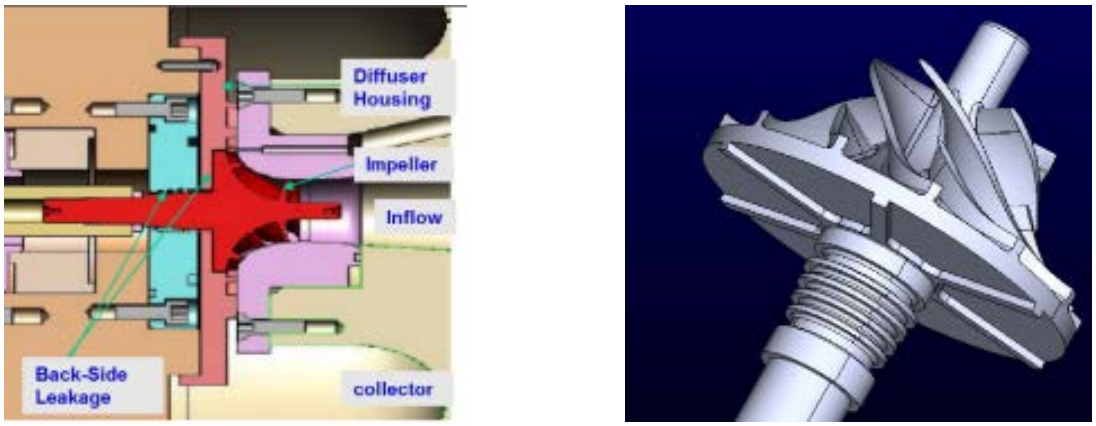

(a) Configuration (b) Impeller

Figure 9: Compressor configuration for Sandia Test [1] and Impeller Geometry (from Barber Nichols Inc.) Showing Pump Out Vanes

The CFD model is shown in Figure 10; a high quality grid with approximately 1.4 M cells for a single passage was generated. The diameter of the impeller wheel is 1.471 inches, tip clearance 0.01 inches, and the design rotational speed is 75,000 RPM. The design inlet temperature is 305.30 K and the design inlet pressure is 7.687 MPa both of which are very close to the critical point of CO2 (304.1 K, 7.37 MPa). The design mass flow rate is 3.53 kg/s. Boundary conditions to the inlet pipe specified the temperature and mass flow while the back pressure is specified at the diffuser exit. For this set of boundary conditions the inlet pressure comes out as part of the simulation and is not specified and may not match the specified test conditions exactly.

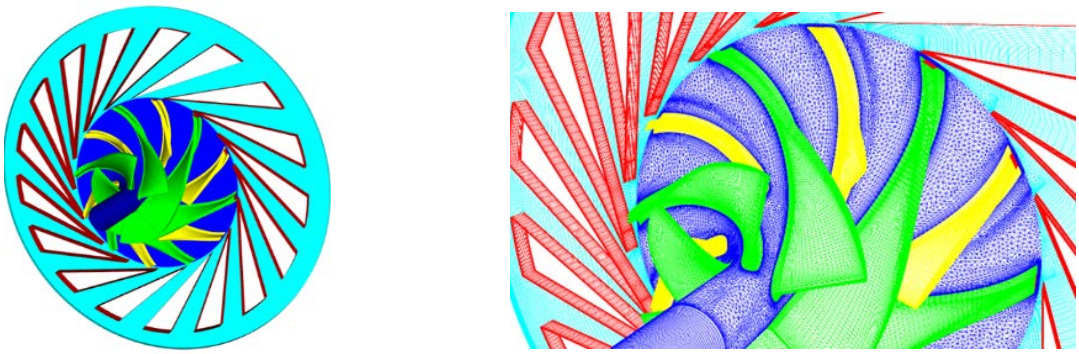

(a) Configuration (b) Impeller

Figure 10: Impeller and Diffuser Configuration in CFD Computation: a) 3-D full wheel geometry, and b) CFD Grid for Impeller and Diffuser

In this section we analyze two-phase effects in compressor flowfields. Phase change is triggered when local conditions become subcritical and do not require the phase to be specified apriori. In particular, whether condensation or cavitation occurs is governed by the local pressure relative to the saturation pressure corresponding to the local temperature and not specified by the user apriori. Calculations were performed at three different inlet conditions; Case 1) Supercritical inlet conditions at inlet temperature of 305.4 K and pressure of 7.843 MPa, Case 2) 2-phase inlet where the inlet is subcritical at a temperature of 290 K and pressure of 5.21 MPa and lastly Case 3) Liquid inlet conditions at a temperature of 295 K at three different pressures of 6.31 MPa, 6.71 MPa, and 7.29 MPa. The location of these different inlet conditions relative to the saturation dome are shown in Figure 11.

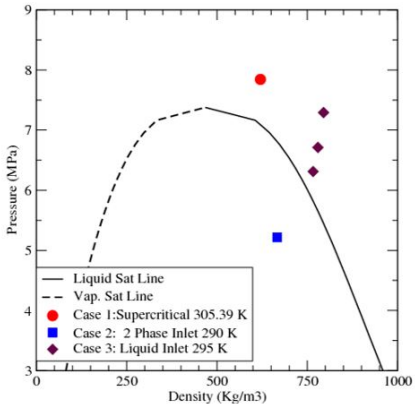

Figure 11: Inlet conditions for the various cases computed shown relative to the saturation dome on a pressure-density plot

Case 1: Phase Change at Supercritical Inlet Conditions

Calculations for this case are performed for an inlet temperature of 305.4 K and pressure of 7.843 MPa (both of which are mildly supercritical). The rotational speed is 55872 RPM, and the mass flow rate is 2.24 Kg/s (5 lbm/s). As the flow accelerated around the leading edge, the temperature drops locally and becomes subcritical as shown in Figure 12. The temperature drops locally to values around 285-289 K at the leading edge suction side. The pressure does not drop as much and remains above the local vapor pressure at these subcritical temperatures. Similarly, we get a low temperature region at the blunt trailing edge of the impeller. Hence a local pocket of liquid condenses both near the leading edge (max volume fraction 2.5%) as well as at trailing edge of the impeller. Isosurface of liquid volume fraction (for a value of 1%) is shown as a white surface in Figure 12(c). The volume of liquid being very small does not affect the performance of the compressor. As the temperature rises, the liquid vaporizes back further downstream.

Presently, the question of whether condensation occurs at near critical conditions at the leading edge of the compressor appears to be an unresolved issue. For example, in Baltadjiev et al. [11] the metastable region at the leading edge of the compressor is qualitatively similar to our condensation zone. However, the authors argue that stable liquid droplets will not form since the time scale for condensation is much smaller than the residence time of the fluid. The present equilibrium phase change model used in our study cannot resolve this point; we are currently working on a non-equilibrium model extension to compare this calculation to

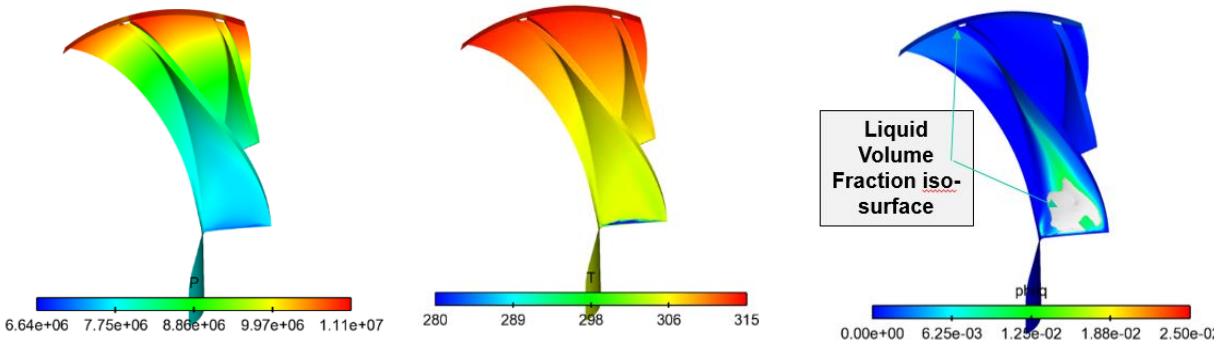

(a) Pressure (b) Temperature (c) Liquid Volume Fraction

Figure 12: Multi-Phase Computation for Supercritical Inlet Temperature of 305.4k at 5 lbm/s: a) Pressure, b) Temperature, and c) Liquid Volume Fraction Iso-surface

Case 2: 2-Phase Inlet Conditions

A more complex calculation with a 2-phase inlet has also been conducted to analyze off-design operation of the compressor; these conditions were chosen to represent potential conditions during start-up where the pressure and inlet temperatures are low. As discussed in Noall and Pasch [3], at start-up the compressor is used as a circulator while heaters raise the temperature to supercritical temperatures. Here the fluid at the inlet is specified at 290 K and 5.21 MPA (close to saturation pressure at 290K), with 20% vapor by volume and 80% liquid by volume; the choice of the 2-phase quality was arbitrary. The rotational speed of the compressor is 53240 and the mass flow rate is 5.736 lbm/s. Phase change to liquid as pressure rises in the compressor is accounted for. Enthalpy rise is substantial and is comparable to single phase calculation. However, the temperature rise is lower and the fluid exits diffuser at subcritical temperatures.

The flowfield in the compressor is illustrated in Figure 13. Unlike the previous case at inlet design temperatures where condensation at the leading edge was triggered, the flowfield for the 2-phase inlet indicates that the liquid will vaporize as the mixture accelerates around the leading edge. Figure 13 c and d show that the density drops and vapor volume fraction increases in a larger region near the leading edge. We also note that since the inlet pressure was slightly lower than the saturation pressure at 290 K, small levels of vaporization occurred in the suction pipe leading to a slightly lower temperature (due to evaporative cooling) and a marginally higher vapor fraction.

The results above indicate that for 2-phase inlet conditions with substantial mass of liquid entering the impeller, the temperature drop of the fluid around the leading edge reduces while the pressure drop continues to be substantial. Consequently, the fluid pressure becomes lower than the local saturation pressure leading to vaporization. We postulate that this characteristic is arising from the reduced compressibility of the fluid when substantial liquid mass is present. The reduced compressibility suppresses the temperature reduction as the fluid accelerates at the leading edge thus leading to cavitation rather than condensation. Hence the impeller begins to exhibit characteristics of a pump at these conditions. As a final note, we point out that as the pressure rises further downstream in the impeller, the vapor condenses back to liquid and the exit of the impeller is primarily liquid.

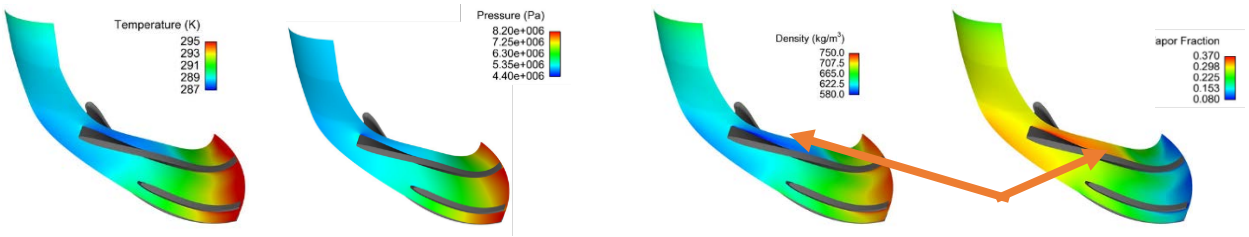

(a) Temperature (b) Pressure (c) Density (d) Vapor Volume Fraction

Figure 13: Flowfield in Impeller for 2-Phase Inlet Calculation at 290K.

Case 3: Subcritical Liquid Inlet Calculation

A more plausible sub-critical condition that may occur during start-up is considered here; we analyze compressed liquid inlet at a temperature of 295 K. The saturation pressure at 295 K is 5.982 MPa. Here we analyze three different inlet pressures at 6.31, 6.71, and 7.29 MPa and determine the potential for phase change at each condition. The rotational speed and mass flow rates are otherwise identical to the earlier Case 2 with values of 53240 RPM and 2.6 Kg/s (5.736 lbm/s) respectively.

Figure 14 illustrates the density in the impeller for the three different inlet pressures for subcritical liquid inlet conditions. At inlet pressure of 7.29 MPa, we observe high liquid density values throughout the impeller indicating no phase change. However as the pressure is reduced to 6.71 MPa, a small region of low

pressure is observed around 75% span at the leading edge. As the pressure is reduced further to 6.61 MPa and we get closer to the saturation pressure, a well-defined region of low density is observed at the leading edge indicating cavitation or vaporization due to pressure drop.

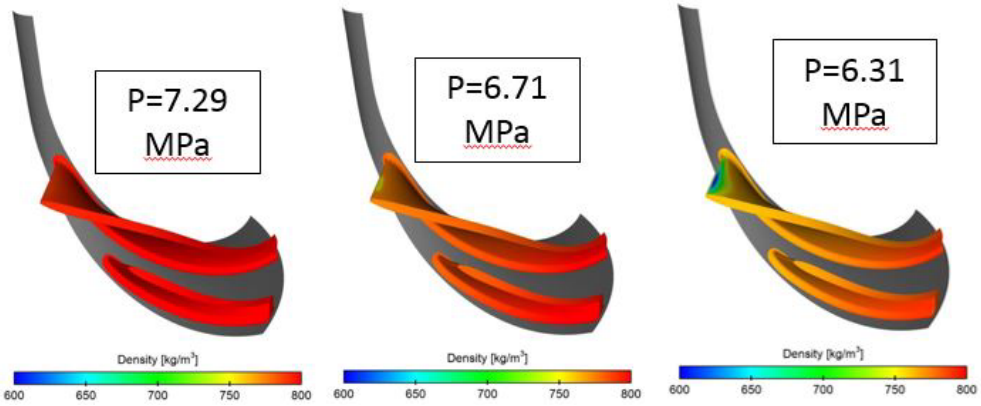

Figure 14: Density contours in impeller at various pressures for subcritical liquid inlet

Phase change due to cavitation is confirmed by making iso-surface plots of vapor volume fraction in Figure 15. At an inlet pressure of 7.29 MPa, no vapor is observed and the entire impeller remains wetted. At 6.71 MPa, cavitation inception is observed in a small region at the leading edge and by 6.31 MPa a well-defined cavitation region in the leading edge is observed. The temperature field in the impeller is shown in Figure 16. We note that as cavitation the fluid temperature drops further due to evaporative cooling effect of the phase change. Indeed, the temperature reduction lowers the saturation pressure and acts to suppress additional cavitation which is a well-known phenomenon in cryogenic turbomachinery.

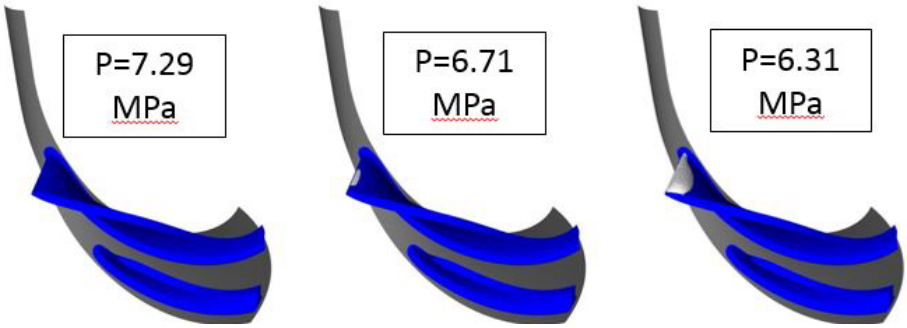

Figure 15: Iso-surface of vapor volume fraction in impeller at various pressures for subcritical liquid inlet

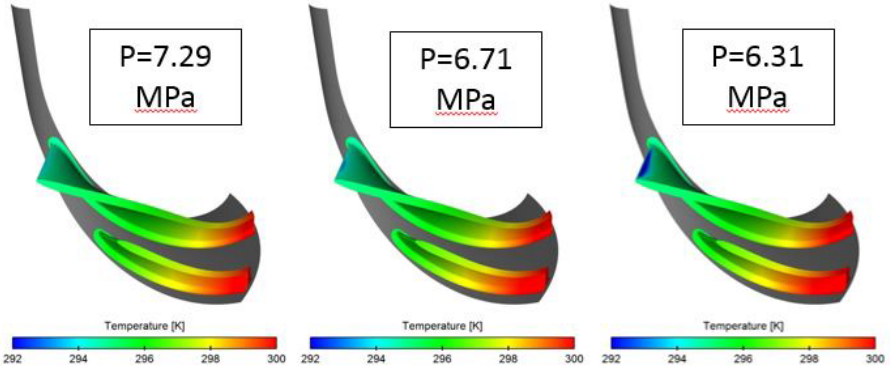

Figure 16: Temperature contours in impeller at various pressures for subcritical liquid inlet

The performance of the compressor at three different pressures is shown in Table 2. We notice that the total pressure and enthalpy rise decrease slightly as the inlet pressure drops. However this decrease in performance is not due to the cavitation. Rather, since the inlet density becomes lower with lower pressure and we are keeping mass flow constant, the inlet velocity increases and thereby increases the flow coefficient. The flow coefficient determines the incidence angle of the incoming fluid streamline to the blade; as the flow coefficient increases slightly the incidence decreases and thereby reduces the head generated by the compressor. Clearly, if the inlet pressure is reduced further and there is more substantial cavitation then performance could potentially reduce due to phase change effects.

Table 2: Performance of the compressor at various inlet pressures for subcritical liquid inlet

Case	Inlet Pressure (MPa)	Inlet Density (Kg/m^3)	ΔP_T (MPa)	Δh (KJ/Kg)
Case 3a	7.292	795.047	5.523	7.560
Case 3b	6.711	779.493	5.394	7.52
Case 3c	6.311	766.182	5.298	7.493

One concern with cavitation in the impeller is the possibility of blade damage and erosion. However in the temperature regime in which the compressor is operating the density ration between the liquid and vapor is much lower (order of 4) compared to other cryogenic systems such as liquid hydrogen pumps where the density ratio is of the order of 70. Thus, the damage from cavitation cloud collapse as the vapor condenses downstream will be mitigated and may not be a critical design issue.

Concluding Remarks

A generalized numerical framework to model phase change at subcritical conditions in CO_2 over a wide range of conditions is presented in this paper. This model is implemented with an advanced numerical framework that features independent mass transport equations for liquid and vapor CO_2, and can also be extended to include contaminants. A table look-up procedure based on the NIST database was implemented for both supercritical and subcritical conditions. A key contribution here is the extension of the look-up procedure to subcritical conditions using saturation curves as bounding lines to distinguish between liquid and vapor properties. Phase change is triggered by the difference between the local values of pressure and saturation pressure and do not require the phase to be specified apriori. This framework can be extended to more complex mixtures of CO_2 and contaminants such as water in the future.

The phase change framework is validated rigorously for condensation in CO_2 using test data in a De Laval nozzle published by Lettieri et al. [9]. Condensation solutions for inlet pressures ranging from 58.96 bar to 84.74 bar with temperatures in a narrow band from 311.99 K to 314.67 K are computed. The computed condensation patterns are compared with flow visualization pictures and condensation onset is quantitatively compared with the test data; in general, the comparisons are very good. The numerically computed Wilson line is compared with the test data. We note that the CFD predictions overall under-predict the test data marginally but the variation with inlet entropy matches the data well with the CFD curve nearly parallel to the test curve. As the inlet entropy gets closer to the critical value, the comparison with the test data gets better because the condensation onset is rapid and the implied time scale in the equilibrium formulation becomes a very good approximation to the non-equilibrium process. The pressure profiles in the nozzle are also compared directly with the test measurements. We observe that at the lower pressures of 58.96 bar and 65.35 bar the pressure comparisons show differences around the condensation onset point. The comparison improves at higher pressures as condensation is enhanced and equilibrium is attained more rapidly.

The phase change model was subsequently demonstrated for the compressor in the Sandia test loop for three different sets of inlet conditions: Case 1) Supercritical inlet conditions at inlet temperature of 305.4 K and pressure of 7.843 MPa, Case 2) 2-phase inlet where the inlet is subcritical at a temperature of 290 K and pressure of 5.21 MPa and lastly Case 3) Liquid inlet conditions at a temperature of 295 K at three different pressures of 6.31 MPa, 6.71 MPa, and 7.29 MPa. For Case 1, with the inlet conditions near the design point the phase change model predicts condensation at the leading edge and trailing edge of the impeller as the temperature profiles drops relatively faster than the pressure making the fluid sub-cooled. However, the phase change characteristics show a dramatic change when the inlet has substantial liquid

mass at subcritical conditions. For Case 2 (two-phase inlet) and Case 3 (liquid inlet), we observe cavitation rather than condensation near the leading edge as the relative variations of pressure and temperature change. For Case 3, with compressed liquid inlet flow, the presence of cavitation is governed by the pressure levels. For pressure levels much higher than the inlet saturation pressure only single phase flow is observed. However if the inlet pressure drops and gets closer to the saturation pressure a distinct cavitation pattern at the leading edge is observed. At these subcritical inlet conditions with liquid inflow, the pressure drop is more than the saturation pressure drop from the lower temperature as the flow accelerates round the leading edge leading to vaporization or cavitation. We postulate that reduced compressibility in liquid suppresses the temperature decrease at these conditions. While cavitation is a concern due to its potential for damage and erosion, the effect of cavitation is mitigated by the fact that the liquid to vapor density ratios at these elevated temperatures are much smaller (order of 4) thus reducing the pressure amplitudes from cavitation collapse.

REFERENCES

[1]. Wright, S. A., Radel, R. F., Conboy, T. M., and Rochau, G. E., "Modeling and Experimental Results for Condensing Supercritical CO2 Power Cycles", SANDIA Report, SAND2010-8840, 2011.

[2]. Pelton, R., Allison, T., Jung, S., and Smith, N. "Design of a Wide-Range Centrifugal Compressor Stage for Supercritical CO2 Power Cycles", GT2017-65172, Proceedings od ASME Turbo Expo 2017, Turbomachinery Technical Conference and Exposition, GT2017, 2017.

[3]. Noall, J.S., and Pasch, J.J., "Achievable Efficiency and Stability of Supercritical CO_2 Compression Systems", *Supercritical CO2 Power Cycles Symposium*, Pittsburg, Pennsylvania, 2014.

[4]. "Fundamentals and Applications of Supercritical Carbon Dioxide (sCO_2) Based Power Cycles", Ed. Klaus Brun, Peter Friedman, and Richard Dennis, Woodhead Publishing Series in Energy, 2017.

[5]. Qian, JW, Privat, R, Jaubert, JN, "Predicting the phase equilibria, critical phenomena, and mixing enthalpies of binary aqueous systems containing alkanes, cycloalkanes, aromatics, alkenes, and gases (N2, CO2, H2S, H2) with the PPR78 equation of state," *Industrial & Engineering Chemistry Research,* 52 (46) (2013) 16457-16490.

[6]. McDonald, J.E., "Homogeneous Nucleation of Vapour Condensation. I. Thermodynamic Aspects", American Journal of Physics, Vol.30,1962, pp.870-877.

[7]. Young, J.B., "The Condensation and Evaporation of Liquid Droplets in a Pure Vapour at Arbitrary Knudsen Number, *Int J Heat Mass Transfer*, Vol. 34, No. 7, pp. 1649-1661, 1991.

[8]. Hosangadi, A. and Ahuja, V., "Numerical Study of Cavitation In Cryogenic Fluids," *Journal of Fluids Engineering*, Vol. 127, pp. 267-281, March 2005

[9]. Lettieri, C., Paxson, D., Spakovszky, Z., Bryanstron-Cross, P., "Characterization of Non-Equilibrium Condensation of Supercritical Carbon Dioxide in a De Laval Nozzle", *J. of Engineering for Gas Turbines and Power*, Accepted for Publication.

[10]. Hosangadi, A., Lee, C.P., Kannepalli, C., and Arunajatesan, S., "Three Dimensional Hybrid RANS/LES Simulations of a Supercritical Liquid Nitrogen Jet", Joint Propulsion Conference & Exhibit, Hartford, CT, Paper No. AIAA-2008-5227, July 2008

[11]. Baltadjiev, N., Lettieri, C., Spakovszky, Z., "An Investigation of Real Gas Effects in Supercritical CO_2 Centrifugal Compressors", Proceedings of ASME Turbo Expo 2014: Turbine Technical Conference and Exposition GT2014, 2014.

[12]. Pecnik, R., and Colonna, P., "Accurate CFD Analysis of a Radial Compressor Operating with Supercritical CO_2", Supercritical CO_2 Power Cycle Symposium, Boulder, Colorado, 2011.

[13]. Ameli, A., Afzalifar, A., Turenen-Saaresti, T., Backman, J., "Effects of Real Gas Model Accuracy and Operating Conditions on the Supercritical CO2 Compressor Performance and Flowfield", Proceedings of ASME Turbo Expo 2017; Turbomachinery Technical Conference and Exposition, GT2017, 2017.

[14]. Xia, G., Sankaran, V., Li, D., and Merkle, C.L., "Modeling of Turbulent Mixing Layer Dynamics in Ultra-High Pressure Flows", 38th AIAA Fluid Dynamics Conf., San Francisco, CA, AIAA 2006-3729, 2006

[15]. Hosangadi, A., Sachdev, J., and Venkateswaran, S., "Improved Flux Formulations for Unsteady Low Mach Number Flows", Seventh International Conference on Computational Fluid Dynamics, Paper No. ICCFD7-2202, Big Island, Hawaii, July 2012.

[16]. Hosangadi, A., Ahuja, V., and Ungewitter, R.J., "Simulations of Rotational Cavitation Instabilities in the SSME LPFP Inducer," Paper No. AIAA-2007-5536, JPC, Cincinnati, OH, July 8 – 11, 2007.

[17]. Arunajatesan, S. and Sinha, N., “Hybrid RANS-LES Modeling for Cavity Aeroacoustics Predictions,” *International Journal of Aeroacoustics*, Vol. 2, No. 1, pp 65-91, 2003.
[18]. NIST: Thermophysical Properties of Fluid Systems. Online Access at http://webbook.nist.gov/chemistry/fluid/

ACKNOWLEDGEMENTS

This work was performed under DoE Phase I and Phase II SBIR grant DE- SC0015856 with Mr. Parrish Galusky as the program monitor. We gratefully acknowledge support from NETL, Morgantown. We would also like to thank Mr. Bob Fuller from Barber Nichols Inc. for providing us with the geometry for the compressor as well as the raw data obtained by BNI as part of their test program. This effort would not have been possible without his help. We also gratefully acknowledge the support provided by Dr. Judy Busby from JB Design and Consulting LLC for helping us analyze and compare the compressor performance data. Last, but not least, we would like to thank Prof. Lettieri for providing us his test data on the De Laval nozzle and giving us his feedback on the CFD comparisons with his test data.